



Multi-mass velocity-map imaging studies of photoinduced and electron-induced chemistry

Claire Vallance^{*a}

Received 00th January 20xx,
Accepted 00th January 20xx

DOI: 10.1039/x0xx00000x

www.rsc.org/

Multi-mass velocity-map imaging (VMI) is becoming established as a promising method for probing the dynamics of a variety of gas-phase chemical processes. We provide an overview of velocity-map imaging and multi-mass velocity-map imaging techniques, highlighting examples in which these approaches have been used to provide mechanistic insights into a range of photoinduced and electron-induced chemical processes. Multi-mass detection capabilities have also led to the development of two new tools for the chemical dynamics toolbox, in the form of Coulomb-explosion imaging and covariance-map imaging. These allow details of molecular structure to be followed in real time over the course of a chemical reaction, offering the tantalising prospect of recording real-time ‘molecular movies’ of chemical dynamics. As these new methods become established within the reaction dynamics community, they promise new mechanistic insights into chemistry relevant to fields ranging from atmospheric chemistry and astrochemistry through to synthetic organic photochemistry and biology.

1. Introduction

Understanding the detailed mechanism of a chemical reaction is a key goal in chemistry. Armed with knowledge of the pathway from reactants to products, chemists can optimise reaction pathways, improve industrial processes, design new drugs and materials, and react to environmental challenges. Unfortunately, probing a chemical reaction mechanism is not straightforward: chemistry occurs on sub-nanometre length scales, firmly within the realm of quantum mechanics, and on ultra-fast (femtosecond) timescales. The majority of mechanistic studies in chemistry rely on indirect methods, piecing together a jigsaw of measurable properties such as product yields, reaction rates, temperature dependences, and isotope effects, together with the predictions of one or more proposed mechanisms¹. Unfortunately, such measurements are averaged over an almost unimaginably huge number of events, washing out many of the more subtle, and interesting, aspects of the reactivity. For certain types of reaction, a much more direct approach is possible, in which reaction mechanisms are studied almost one molecule at a time through measurements of the product scattering distribution². Such techniques are the subject of the present review.

A chemical reaction can be defined as any process in which chemical bonds are made or broken. The energy required to initiate a chemical reaction may either result from a collision (‘thermal initiation’), or by absorption of a photon (‘photoinitiation’). The

latter, photoinitiated, processes are sometimes referred to as ‘half collisions’. As early as 1933, a number of researchers³ recognised that for gas-phase reactions in which the initial conditions are well defined, measurement of the product scattering distribution can provide a great deal of direct information on the reaction mechanism. The scattering distribution provides a unique signature for a chemical process, and can be analysed to determine the forces and energetics that drive chemical reactivity. Over the past few decades, much effort has been spent on developing experimental methodologies for measuring reaction product scattering distributions. Control over reactant velocities and internal states is achieved using molecular beam techniques. A molecular beam of well-defined energy can be crossed with another molecular beam to study bimolecular reactions or other scattering processes, with an electron beam to study electron-molecule collisions, or with a laser beam to study photoinitiated chemistry. Early methods of measuring the scattering distribution depended on recording a series of one-dimensional projections using either Doppler spectroscopy⁴ or time-of-flight measurements⁵. However, these have almost universally been replaced by two-dimensional and even three-dimensional methods based on velocity-map imaging, the subject of this review. When studying photoinitiated processes, laser pump-probe methods allow precise control over both the time at which reaction is initiated and the identity and even internal quantum state(s) of the reaction products that are detected in a given experiment. With the advent of femtosecond lasers, it is now possible to follow chemical reactions directly on their own timescale, and to watch the scattering distribution evolve as the reaction proceeds. With the recent development of ultra-fast imaging methods, we are very close to being able to record ‘molecular movies’ of chemical change.

In the following, we introduce the technique of velocity-map imaging and explain how to interpret the scattering distribution images in

^a Department of Chemistry, University of Oxford, Chemistry Research Laboratory, 12 Mansfield Rd, Oxford OX1 3TA, UK

^b † Footnotes relating to the title and/or authors should appear here.

Electronic Supplementary Information (ESI) available: [details of any supplementary information available should be included here]. See DOI: 10.1039/x0xx00000x

order to gain insight into chemical reaction mechanisms. We will consider a variety of examples in which these methods have been used to study both photoinitiated and electron-initiated chemistry, including some recent studies on the femtosecond timescale.

2. Velocity-map imaging

First developed by Parker and Eppink⁶ in 1997, building on previous work by Chandler and Houston⁷, velocity-map imaging (VMI) has revolutionised experimental work in the field of chemical reaction dynamics by allowing the complete scattering distribution for a chosen reaction product to be imaged directly in a single measurement. VMI has most commonly been used to investigate photoinitiated processes, but has also been used extensively to study bimolecular processes, including inelastic collisions⁸, neutral-neutral reactions⁹, and ion-molecule reactions¹⁰. For the purposes of the present discussion, we will focus on photoinitiated and electron-initiated processes.

Figure 1 shows a schematic of a simple velocity-map imaging experiment designed to record the scattering distribution arising from a photoinitiated event. To study electron-molecule collisions, the two laser beams are replaced with a single pulsed electron beam. The apparatus is essentially a modified time-of-flight mass spectrometer, in which the ions to be detected are either formed directly in the chemical process under study, or by ionising neutral reaction products from the process. To enable imaging, the particle-counting detector used in a conventional time-of-flight mass spectrometer is replaced by a position sensitive imaging detector.

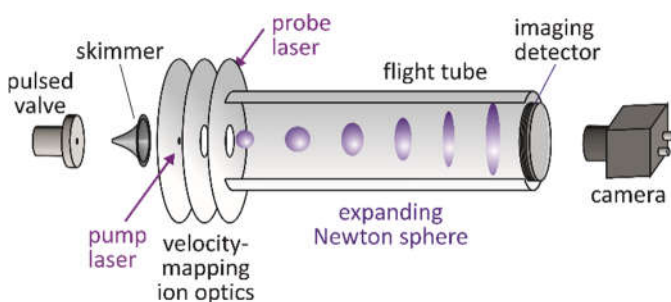


Figure 1: Schematic of a velocity-map imaging experiment for studying photoinitiated processes.

The molecule of interest is prepared in a supersonic expansion, which yields internally cold molecules with a narrow and well-defined velocity distribution. The resulting molecular beam is collimated by a skimmer, before entering a set of electrostatic optics known as a “velocity-map imaging lens”. Here, the beam is intersected either by an electron beam or by two laser beams, depending on the process to be studied. In the former case, ions are produced directly as a result of the electron-molecule collisions - examples of such processes will be discussed in Section 4. In the latter case, the first laser beam, known as the ‘pump’ or ‘photolysis’ beam, initiates the photolysis reaction of interest, generating neutral reaction products that must be ionized by the second, ‘probe’, laser pulse in order to

be detected. This can either be done in a state-selective way, in which a carefully tuned laser selectively ionizes a specific fragment in a specific quantum state, or using a more ‘universal’ approach in which all fragments are ionised. Ionization methods are discussed further in Section 2.2.1.

In all cases, the reaction products fly out in various directions from the crossing point between the molecular beam and the electron beam or pump laser beam. The resulting scattering distribution is often described in terms of a series of concentric ‘Newton spheres’, with each Newton sphere comprising the expanding sphere of products with a given speed and chemical identity. The angular distribution within each Newton sphere is not necessarily isotropic, and often contains a great deal of information on the dynamics of the chemical process under study.

To measure the scattering distribution, the product ions are accelerated along the flight tube towards the position-sensitive detector by an electric field maintained within the velocity-mapping ion optics. All ions with a given charge z are accelerated to the same final kinetic energy,

$$zV = \frac{1}{2}mv^2 \quad (1)$$

where V is the acceleration potential, m is the mass of the ion, and v is the final velocity component of the ion along the time-of-flight axis. We see from Equation (1) that the final velocity of the ion depends on its mass-to-charge ratio. Ions with different mass-to-charge ratios therefore become separated in time as they traverse the flight tube and arrive at the detector at characteristic times. By recording the arrival times of the ions, their mass-to-charge ratios, and therefore the identities of the reaction products, can be determined.

In addition to accelerating the ions along the flight tube, the velocity-mapping field is carefully tuned to map the velocities of individual ionized products very precisely onto the position-sensitive detector. The field is tuned to correct for any blurring effects of the finite interaction volume between the crossed beams, such that the velocity distribution for a given product is faithfully mapped onto the detector. In the simplest form of velocity-map imaging, the field also focuses the ion distribution along the time-of-flight direction, so that the Newton spheres arrive as ‘Newton pancakes’ at the detector. The measured ‘crushed’ images are two-dimensional (2D) projections of the full three-dimensional (3D) scattering distribution. A number of integral transforms are in widespread use to recover the 3D scattering distribution from the 2D projection in order to analyse the data quantitatively¹¹. The majority of these employ some variation on the inverse Abel transform, which requires that the original 3D scattering distribution has cylindrical symmetry and returns a 2D slice through the centre of the ‘reinflated’ 3D distribution. The required cylindrical symmetry is present in most applications of VMI: in photodissociation studies, the scattering distribution is cylindrically symmetric about the polarisation axis of the linearly polarised photolysis light, while in bimolecular or electron-molecule scattering, the distribution is cylindrically symmetric about the relative velocity vector of the two particle beams.

It is also possible to use the velocity-mapping electric field to stretch out the Newton spheres along the time-of-flight axis and to record either the complete three-dimensional distribution or a single central

slice directly¹². This 'slice imaging' approach yields the same information as a complete crushed image, without the need for an image inversion step. The various approaches are illustrated schematically in Figure 2.

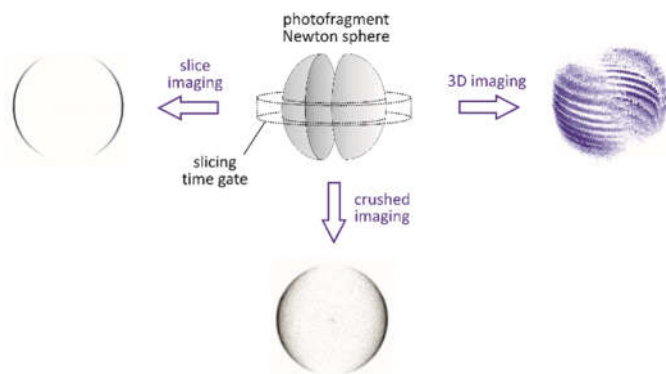


Figure 2: Recording a scattering distribution in crushed, sliced, and 3D sliced imaging modes

The detector comprises a set of microchannel plates coupled to a phosphor screen. The microchannel plates convert each ion into a pulse of electrons, which generates a brief localised flash of light on the phosphor screen. The images of the scattering distribution for each ion appearing on the phosphor are captured by a CCD or CMOS camera and output to a PC for further processing and analysis. A number of data acquisition and image-processing algorithms have been developed in order to locate the arrival position of each ion as accurately as possible, and therefore to maximise the velocity resolution of the images¹³. To obtain sufficiently good statistics, images are typically accumulated over several thousand acquisition (i.e. laser pump-probe or time-of-flight) cycles in order to build up the scattering distributions of thousands of individual chemical events.

VMI has multiple advantages over earlier experimental methods for measuring scattering distributions, including a vast increase in the data acquisition rate as well as improved product speed and angular

resolution. As a result, it replaced these techniques in most chemical dynamics laboratories within a decade.

2.1 Interpreting a velocity-map image

Over the first ten years or so following its discovery, VMI provided enormous insight into the photoinduced and collision-induced dynamics of a wide range of small (typically two or three atom) molecules. Examples of velocity-map imaging applied to photodissociation of diatomic and triatomic molecules can be found in a number of review articles and books¹⁴.

To give the reader some insight into the information contained in a velocity-map image, consider the simplest photoinitiated reaction, namely the photo-induced dissociation of a diatomic molecule into its two constituent atoms. The principles outlined in the following apply to photoinitiated chemical reactions, and also, with some caveats, to the electron-molecule collisions and Coulomb-explosions that will be discussed later on in Sections 4 and 5. Figure 3(b) shows a velocity-map image of Cl atoms formed in the 308 nm photolysis of the Cl₂ molecule¹⁵. As noted earlier, the 'raw' image, as acquired directly in the experiment, is a two-dimensional (2D) projection of the full three-dimensional (3D) scattering distribution, with the radial coordinate containing information on the speed of the atomic products and the angular coordinate describing their angular distribution. In Figure 3(c), we show the Abel-inverted image, which represents a slice through the centre of the 3D scattering distribution. We note that the Cl atoms form a single Newton sphere, with a markedly anisotropic angular distribution. We explain these two features in the following.

During the photodissociation process, Cl₂ molecules are excited from their bound X¹Σ electronic ground state to the unbound C¹Π excited state. As shown in Figure 3(a), the excited state contains no minimum corresponding to a stable chemical bond (i.e. there is no energetic barrier to dissociation), and the molecule therefore rapidly follows a 'downhill' energy pathway on the excited-state potential energy curve to separate into two Cl atoms. The appearance of the image can be explained completely in terms of (i) the principles of conservation of energy and momentum, and (ii) the symmetries of the two electronic states involved in the dissociation.

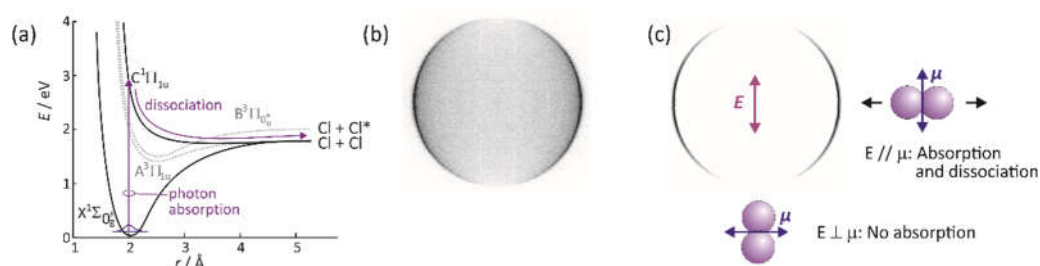


Figure 3: Velocity-map imaging of Cl₂ photodissociation at 308 nm: (a) potential energy surfaces involved in the dissociation; (b) crushed velocity-map image; (c) Abel inverted image. The arrow in the centre of the Abel-inverted image shows the polarisation of the photolysis laser, and the molecules to the right of and below the image show the interaction of the photolysis polarisation vector with the C ← X transition dipole. Values reported in the literature^{15,16,17,18,19,20} for the photolysis β parameter (see Equation (2)) for this dissociation are between -0.88 and -1.0.

2.1.1 Radial distribution of the image

The energy $h\nu$ of the photolysis light, and the energy $D_0(\text{Cl}_2)$ required to break a Cl–Cl chemical bond, are both well defined. The ‘leftover’ energy, $E_{\text{avail}} = h\nu - D_0(\text{Cl}_2)$, can be released into translational and/or internal energy of the reaction products as they fly apart. In the present example, the two products are Cl atoms in their $^2\text{P}_{3/2}$ electronic ground state, so all of the available energy is released into translation. Conservation of momentum has the consequence that both atoms must be formed with equal and opposite momenta, which for two atoms of equal mass requires that the available energy is split equally between the kinetic energies of the two atoms. The two atoms are therefore formed with a single well-defined speed, which gives the image the appearance of a single ‘ring’ or Newton sphere. Intensity inside the outer ring of the image in the raw image arises due to the projection of the three-dimensional Newton sphere onto the plane of the detector, and disappears in the Abel-inverted (‘central slice’) image. Note that when a more complex molecule dissociates, the available energy can be released into rotation or vibration of the fragments, in addition to translation or electronic excitation. We will see many examples of this in the following sections. The fragment speed distribution can be determined quantitatively by integrating the image over the angular coordinate.

2.1.2 Angular distribution of the image

The angular distribution within a Newton sphere is not usually isotropic, and often contains a great deal of information on the dynamics of the chemical process under study. In the present case, the angular distribution of the atoms results from the interaction between the linearly polarised pump light and the transition dipole moment for the transition from the ground state to the excited state. The transition in molecular chlorine is from the $^1\Sigma_{\text{Og}}^+$ ground state to a $^1\Pi_{1\text{u}}$ excited state. Electron density moves from a σ to a π molecular orbital during the transition, i.e. in a direction perpendicular to the bond axis, and the transition is therefore known as a *perpendicular transition* (in contrast, a σ to σ excitation would involve a *parallel transition*). Effecting the required movement of electron density requires a component of the electric field of the light perpendicular to the bond. Prior to excitation, the Cl_2 molecules within the molecular beam are randomly oriented. As shown in Figure 3(c), molecules that happen to be aligned with their bond axes perpendicular to the polarisation vector of the excitation light will preferentially absorb the light and dissociate^{16,17,18,19,20}, while those aligned with no component of their transition dipole along the polarisation vector cannot absorb the laser radiation, and consequently do not dissociate. This gives rise to the observed $\sin^2\theta$ distribution of the product atom velocities about the polarisation vector of the photolysis light. Analysis of the angular distribution of a velocity-map image often allows the electronic states involved in the reaction pathway to be assigned unambiguously. In general, the angular distribution $P(\theta)$ of the photofragment velocities relative to the polarisation vector of the photolysis light can be described by the following expression²¹:

$$P(\theta) = 1 + \beta P_2(\cos\theta) \quad (2)$$

where $P_2(\cos\theta)$ is a second Legendre polynomial in $\cos\theta$ (with θ the angle between the photolysis polarisation vector and the fragment velocity vector). The parameter β , sometimes known as the

‘photolysis beta parameter’ can take values between -1 and $+2$, with -1 corresponding to a pure perpendicular transition (yielding a $\sin^2\theta$ angular distribution) and $+2$ corresponding to a pure parallel transition ($\cos^2\theta$ angular distribution).

To summarise:

- (i) the radial distribution of a velocity-map image yields insight into the way in which the energy available to the products is partitioned amongst the various available degrees of freedom – translation, rotation, vibration, and electronic excitation. In simple cases, usually involving dissociation of diatomic or triatomic molecules, detailed analysis of the radial distribution in light of the principle of conservation of energy yields the product internal quantum state distributions almost directly.
- (ii) The angular coordinate of an image provides information on the symmetries of the electronic states accessed during the bond-breaking process, and allows these states to be identified.

2.1.3 Additional information

It is worth noting that as well as information on the electronic states involved in the process under study, the angular distribution of a velocity-map image can also provide information on the timescale over which the process occurs. For example, the angular distribution of the Cl atomic products of Cl_2 photodissociation were shown to have a $\sin^2\theta$ distribution relative to the polarisation vector of the photolysis light, as a result of the perpendicular transition from the ground state to the excited state from which dissociation occurs. If instead of observing the expected $\sin^2\theta$ distribution, we had seen a much more isotropic distribution, we could have inferred that the excited state must survive for several rotational periods before dissociating into atoms, such that the expected correlation between the polarisation vector of the excitation light and the scattering direction of the atoms is lost. A similar loss of anisotropy can arise when the structure of the molecule changes significantly prior to dissociation.

For completeness, as an ‘extra for experts’ in the context of the present review, if the rotational or electronic angular momentum vectors of the scattered products have some preferred alignment or orientation, then the probe step becomes sensitive to the polarisation of the probe laser. Recording images for different probe polarisations then allows the angular momentum distribution to be determined. Explaining these polarisation effects quantitatively has been covered in detail elsewhere²² and is beyond the scope of this review, but an example of such an effect is shown in Figure 4. The figure shows images of O(^1D) atoms formed in the 157 nm photolysis of molecular oxygen^{23,24}. Excitation of O_2 at 157 nm leads to dissociation via a parallel transition from the ground state to the $\text{B}^3\Sigma_{\text{u}}^-$ state. The breaking bond can be thought of as being formed from the $2p_z$ orbitals of the two atoms. As the bond breaks, the $2p_z$ orbitals point preferentially along the original bond direction, parallel to the velocity vectors of the departing atoms and to the polarisation vector of the photolysis light (see Figure 4(b)). This leads to different detection efficiencies for the atoms when the probe laser is polarised parallel to or perpendicular to the photolysis laser. The effect of this on the images is shown in Figure 4(a).

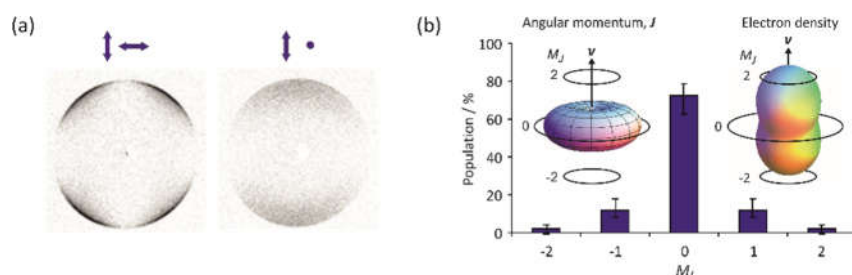


Figure 4: (a) Polarisation of the electronic angular momentum in the $O(^1D_2)$ fragments formed during photolysis of O_2 leads to a dependence of the atomic detection efficiency on the polarisation of the probe laser. This is shown for $O(^1D_2)$ atoms detected by REMPI via the 1P_1 Rydberg state, with pump and probe laser polarisations shown above the images; (b) the images can be analysed to determine the angular momentum polarisation, which corresponds to a non-statistical population of atomic M_j states, as well as the electron density distribution in the recoiling atom. Figures adapted from references 23 and 24.

2.2 Velocity-map imaging studies of larger molecules

In small molecules, the rotational and vibrational energy levels tend to be fairly widely spaced. When this is the case, for a given total available energy the products formed in different quantum states will have measurably different translational energies. This leads to well-resolved Newton spheres in the velocity-map images, each corresponding to one of the populated product quantum states. As molecular size increases, the energy-level spacing becomes progressively smaller, to the point where structure corresponding to individual quantum states can eventually no longer be resolved. For this reason, in the early days of VMI, it was thought that the method was only likely to be useful for studying diatomic and triatomic molecules, and that imaging studies on larger molecules would simply result in unanalysable 'blobs'. As practitioners of VMI became more adventurous, however, it was found that this was simply not the case. Even relatively large polyatomic molecules often yield quite structured, and therefore information-rich, images. Figure 5 shows some examples of such images.

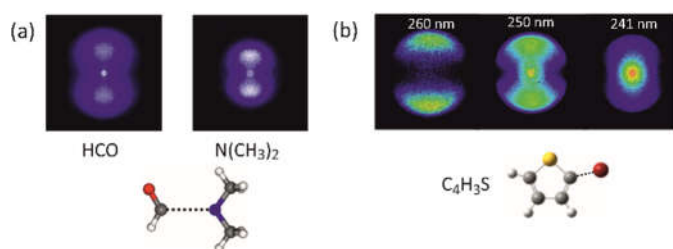


Figure 5: Velocity-map images for 'large' molecules (a) HCO and $N(CH_3)_2$ products of the 193 nm photolysis of dimethylformamide³⁸; (c) C_4H_3S products of the photolysis of bromothiophene at three different wavelengths in the ultraviolet⁴⁴. The breaking bond is indicated by a dotted line in each case.

The discovery that VMI has the potential to reveal reaction pathways in much more complex chemical systems than originally thought was extremely exciting, but also immediately presented a number of experimental challenges. These relate primarily to the rapid increase in the number of possible reaction pathways with increasing molecular size. Absorption of a photon by a very small molecule

typically initiates breaking of a single bond, yielding two momentum-matched fragments. This has the result that by imaging only one fragment, the scattering distribution of both fragments is known via momentum conservation. Often, one or other of the fragments is detected quantum-state selectively in order to investigate how the quantum state distributions of the two fragments are correlated. This requires multiple experiments, but is still a well-defined process that can be carried out within a reasonable period of time to yield a complete picture of the dynamics.

In contrast, photofragmentation of a large molecule often proceeds via multiple fragmentation pathways, leading to numerous different products. Detection of a single product now provides only a small part of the story, and certainly cannot give anything like a complete understanding of the fragmentation dynamics. The ability to detect all fragments is therefore highly desirable. However, laser-based quantum-state-resolved detection schemes have often not been developed for larger molecules, and even if they have, the enormous number of accessible quantum states makes a state-resolved study a daunting prospect. To obtain the greatest amount of information possible from a velocity-map imaging experiment within this new regime, it was clear that a change of approach was needed. Studying larger chemical systems requires a shift in focus away from understanding chemical dynamics at the detailed quantum-state-resolved level, and towards gaining a 'bigger picture' understanding of the various competing reaction channels. The new goal is to develop the ability to image the (non-quantum-state-resolved) scattering distribution of multiple reaction products within a single experiment. Two experimental developments were required in order to achieve this: universal ionization schemes; and multimass imaging.

2.2.1 Universal ionization schemes

Molecular ionization thresholds are typically around 10 eV or higher. Direct single-photon ionization is challenging at such energies, requiring photons in the soft X-ray region, where lasers are not commercially available. Instead, most previous velocity-map imaging studies ionized the fragment of interest state-selectively using a method known as Resonance-Enhanced Multi-Photon Ionization (REMPI), in which one or more photons are used to excite the fragment to an intermediate state (the resonant step), and a

further photon or photons ionizes the molecule from this intermediate state. Employing REMPI detection requires a good understanding of the spectroscopy of the species under study, and a high-power pulsed laser to drive the required multi-photon transitions. The approach is ideal for a small-molecule study, allowing each quantum state of the newly-formed reaction products to be ionized and detected separately. However, for larger molecules the much larger number of quantum states, correspondingly more complicated spectra, and tendency to dissociate into multiple fragments when exposed to high-intensity laser pulses makes state-resolved detection a rather daunting prospect.

While soft X-ray lasers are not commercially available, there are a number of frequency conversion methods that allow the required wavelengths to be generated in a table-top setup. In our own laboratory, we use a combination of conventional frequency doubling and tripling optics and high harmonic generation in an inert gas cell²⁵ to generate the ninth harmonic of a Nd:YAG laser, which has a fundamental wavelength of 1064 nm. This yields photons with a wavelength of 118 nm and an energy of 10.48 eV, sufficient to ionize most, though not all, of the fragments generated in a photodissociation event. Free electron lasers are also becoming more easily accessible as a source of high-energy photons, and are increasingly being used in velocity-map imaging studies. Electron ionization is also being investigated as a possible alternative to photoionization for future studies, though this approach tends to lead to a high degree of dissociation, as we will show in Section 4.

2.2.2 Multi-mass detection

As noted earlier, a velocity-map imaging instrument is essentially a modified time-of-flight mass spectrometer, with ions of different mass-to-charge ratio becoming separated in time as they traverse the flight tube from the ion source region to the MCP/phosphor screen detector. When only one product fragment is to be detected in a given experiment, one can time-gate either the microchannel plates or the camera to the arrival time of the ion of interest in order to detect only the signal from this ion, and to record the corresponding velocity-map image. With a typical repetition rate of 10 Hz for the laser pump-probe cycle that initiates reaction and ionizes the products, a standard (few tens of Hz) frame-rate CCD camera is entirely adequate for such measurements.

The situation changes dramatically when one wants to image all of the fragments formed in a particular laser pump-probe cycle. Each ion time-of-flight signal has a duration of a few nanoseconds, and all of the fragments typically arrive at the detector within a few tens of microseconds. Cameras capable of recording multiple images on a few-microsecond timescale with few-nanosecond exposure times are not widely available. It is of course possible to employ a standard CCD camera and to perform multiple experiments of the type described above, in which a different product is imaged in each experiment. However, ideally one would detect and image all of the masses on each time-of-flight cycle.

As a first foray into the arena of time-resolved multi-mass VMI, in the late 2000s we carried out some early proof of concept experiments on the 193 nm photodissociation of dimethyldisulphide using a commercially available frame-transfer CCD camera (Dalsa

Zenith)²⁶. The camera allowed up to 16 images to be acquired at user-defined exposure times and stored on-chip before readout. Exposures could be programmed with 5 ns timing precision, with a minimum exposure time of 10 ns and a maximum of a little over 1 μ s. Figure 6 shows images of the S^+ , SC^+ , and S_2^+ products formed in these experiments. Images of each fragment were recorded on every time-of-flight cycle, and the final images are summed over approximately 1000 experimental cycles.

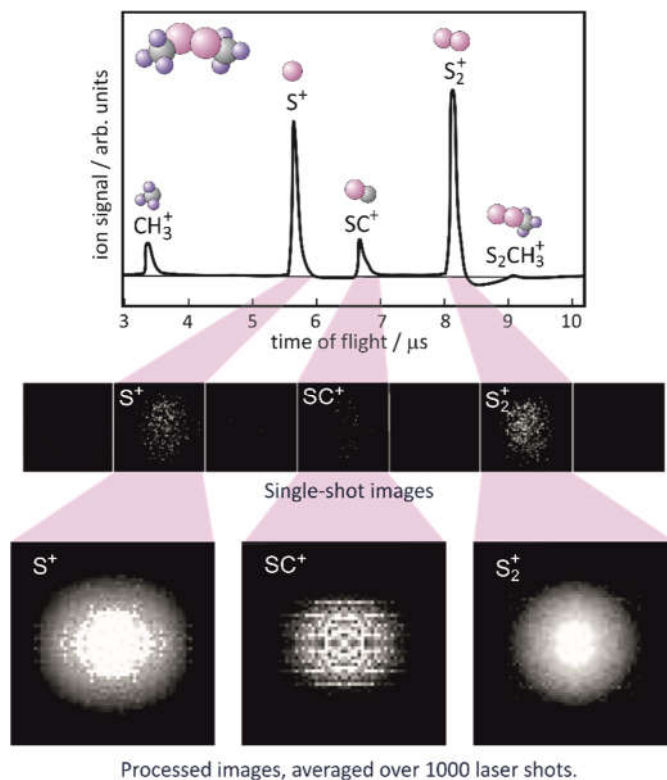


Figure 6: Velocity-map images of the photofragments arising from 193 nm photolysis of dimethyldisulphide, recorded with the DALSA camera: the first time-resolved multi-mass VMI experiment²⁶.

While these experiments demonstrated that time-resolved multi-mass velocity-map imaging is possible, frame-transfer CCDs are not a good long-term solution for such applications. The number of fragments for which images can be recorded in a given experiment is limited by the number of on-chip memory registers within each pixel, and increasing the amount of 'real estate' on the chip dedicated to memory registers comes at the cost of reducing the amount available for photodetection, with a corresponding reduction in the sensitivity of the camera. It is also necessary to know in advance when each product fragment will arrive at the detector, in order to program the exposure times. Finally, the number of pixels in cameras of this type is often quite limited – only 64 x 64 in the camera used for the experiments described above.

Over the past ten years or so, CCD technology has been replaced to a large extent by CMOS pixel technology. Following the success of the proof-of-concept work outlined above, we worked with the CMOS image sensor group at the Rutherford Appleton Laboratory to develop the Pixel Imaging Mass Spectrometry (PIImS) camera²⁷.

The PImMS sensor is an event triggered CMOS sensor with 'intelligent' pixels that can record both the position and time at which a signal is detected, with a time resolution of 12.5 ns. The result is an (x, y, t) data point for each detected ion, and the resulting data set can be processed and analysed to reconstruct both the time-of-flight mass spectrum (by integrating over the x and y coordinates), and velocity-map images for each ion (by extracting the data corresponding to the relevant time window). Over the past five years or so, the PImMS sensor has been used for a wide variety of velocity-map imaging experiments in laboratories around the world, some of which will be highlighted in the remainder of this review.

Several other specialised time-resolved CMOS sensors with similar functionality to the PImMS sensor have been developed²⁸, the most prominent of which is the TimePix sensor²⁹. Originally developed by a large consortium based at CERN for applications in particle physics, the TimePix sensor is increasingly finding applications within the VMI community³⁰.

Having established the methodology for universal ionization and multimass imaging, it is now possible to study the dynamics of large molecules in detail. In the following sections we explore examples of photoinduced and electron-induced chemistry studied by multi-mass velocity-map imaging, highlighting some of the novel experimental approaches that multi-mass imaging technology has enabled.

3. Photoinduced chemistry

The development of multi-mass velocity-map imaging over the past decade has broadened the application of VMI techniques considerably, making it possible to study a variety of molecular systems of widespread interest to a broad audience of chemists. Photoinitiated chemical reactions are important in areas of science ranging from atmospheric chemistry and astrochemistry through to synthetic organic chemistry, photobiology, and photomedicine. Velocity-map imaging is very well suited to understanding the

dynamics of some of the underlying fundamental bond-breaking processes involved in such systems. In the following examples, we consider carbon-halogen bond cleavage in neutral and ionized alkyl halides, breaking of a model peptide bond, and the retro-Diels-Alder reaction. Some of these studies employed the PImMS camera to record all fragments simultaneously, while in others the images were recorded sequentially using a conventional CCD camera.

3.1 Breaking of a carbon-halogen bond

Photodissociation of the C-I bond in methyl iodide was the process studied in the very first demonstration of ion imaging in Chandler and Houston's ground-breaking 1987 paper⁷. Following 266 nm excitation, methyl iodide was known to dissociate via two different channels, leading to CH_3 radical products partnered by ground state $\text{I}(^2\text{P}_{3/2})$ or spin-orbit excited $\text{I}(^2\text{P}_{1/2})$, respectively. The energetics for both channels were already well established [REF], making this an ideal test system for the first imaging experiment, and indeed something of a benchmark system for subsequent velocity-map imaging studies. Building on the work of other authors³¹, we have recently carried out a multimass VMI study of the photodissociation of methyl iodide and ethyl iodide at various wavelengths within their first electronic absorption bands³². The accessible electronic states for the two molecules within these bands are shown schematically in Figure 7(a). Example velocity-map images are shown in Figure 7(b) for the alkyl and iodine products of photolysis at 266 nm. The smaller size of the images for the heavier atomic iodine fragments relative to the methyl and ethyl fragment images reflects the momentum matching between the two departing fragments, i.e. $m_{\text{I}} v_{\text{I}} = -m_{\text{Me/Et}} v_{\text{Me/Et}}$, with m_x and v_x the mass and velocity of the respective fragment. The images can be analysed to yield the total translational energy distributions, angular distributions, and branching ratios into the I and I^* product channels. The measured distributions are readily rationalised in terms of three competing dissociation mechanisms. The dominant excitation for both methyl iodide and ethyl iodide within the wavelength region studied is a parallel transition to the

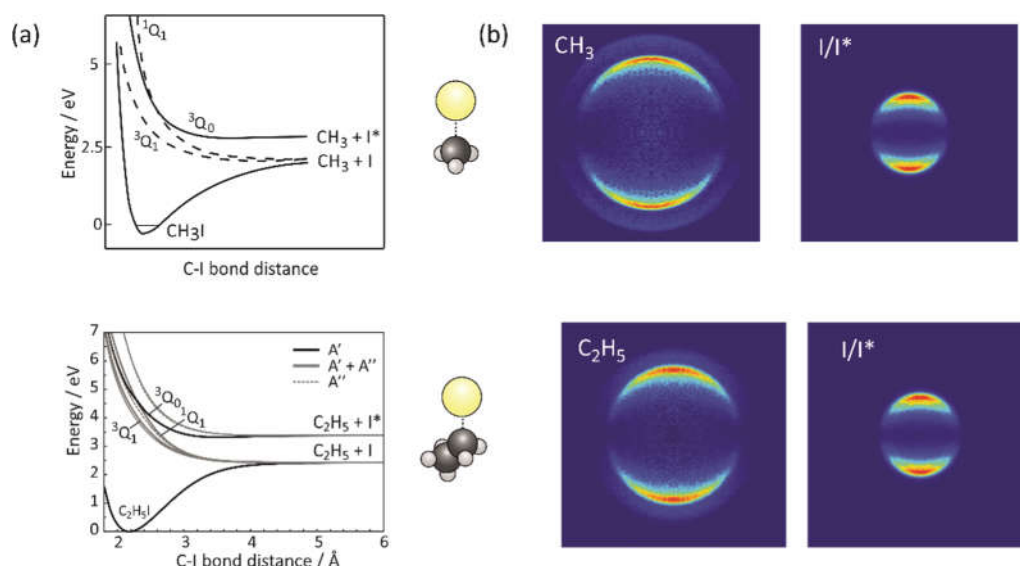
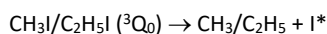
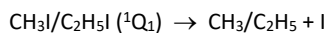


Figure 7: Methyl and ethyl iodide photolysis: (a) accessible electronic states for CH_3I (top) and $\text{CH}_3\text{CH}_2\text{I}$ (bottom); (b) velocity-map images for alkyl and atomic iodine fragments of CH_3I (top) and $\text{CH}_3\text{CH}_2\text{I}$ (bottom) following 266 nm photolysis. The breaking bond is indicated by a dotted line in each case. Figures adapted from reference 32.

3Q_0 state (as defined using the notation introduced by Mulliken³³). This state either dissociates directly to form an alkyl fragment partnered by a spin-orbit excited iodine atom:



or undergoes non-radiative population transfer to the 1Q_1 state to yield an alkyl fragment partnered by ground-state iodine:



The latter dissociation pathway leads to a significant degree of internal excitation in the alkyl radical fragments. The velocity resolution in the methyl iodide images is sufficient to assign this excitation to the ν_1 symmetric stretch and umbrella modes.

In addition to these two major dissociation pathways, minor dissociation pathways were also observed, corresponding to perpendicular transitions to the 1Q_1 or 3Q_1 states, followed by direct dissociation on these states. Both yield a methyl or ethyl fragment partnered by ground state iodine.

3.2 Cleavage of a model peptide bond

Photodissociation studies on amides provide a stepping stone to understanding the behaviour of energised peptide bonds within proteins, providing insight into photostability and photodamage mechanisms in biomolecules. N,N-dimethylformamide (N,N-DMF), $\text{N}(\text{CH}_3)_2\text{CHO}$, provides a useful model for investigating peptide bond fragmentation dynamics, and had been studied by a number of other

authors^{34,35,36,37} prior to our recent multimass VMI study³⁸. Figure 8(a) shows cuts through the first few adiabatic potential energy surfaces for dissociation of N,N-DMF along the C-N, N-CH₃ and C-H bond coordinates. Figure 8(b) shows velocity-map images and product speed distributions extracted from the images for the observed fragmentation products following photolysis at 193 nm and ionization of the resulting product fragments at 118 nm.

Cleavage of the N-C 'peptide' bond is expected to yield $\text{N}(\text{CH}_3)_2$, with $m/z = 44$, and HCO, with $m/z = 29$. If we probe the products with 193 nm (rather than 118 nm) light then we do see a clear signal at $m/z = 44$. However, with 118 nm probe light the $m/z = 44$ signal is replaced with signals at $m/z = 43$, 42, and 16, indicating that the $\text{N}(\text{CH}_3)_2$ products undergo dissociative ionization at this wavelength. Complication of the signals in this way is one of the downsides of using very short wavelength probe radiation to effect single-photon ionization of the reaction products. In the case of H or H₂ loss, dissociation of the parent ion has only a very small effect on the measured velocity of the resulting NC_2H_5^+ and NC_2H_4^+ ions, since conservation of momentum has the consequence that the very light H or H₂ carries away almost all of the kinetic energy associated with the secondary dissociation step. Perhaps surprisingly, dissociation of $\text{N}(\text{CH}_3)_2^+$ to form NH_4^+ , which requires a significant structural rearrangement, also appears to result in very little additional kinetic energy release. The differing appearances of the images for the various fragments primarily reflect the fact that the most likely dissociative ionization channel for a given parent ion depends on its internal energy. The most highly internally excited fragments yield

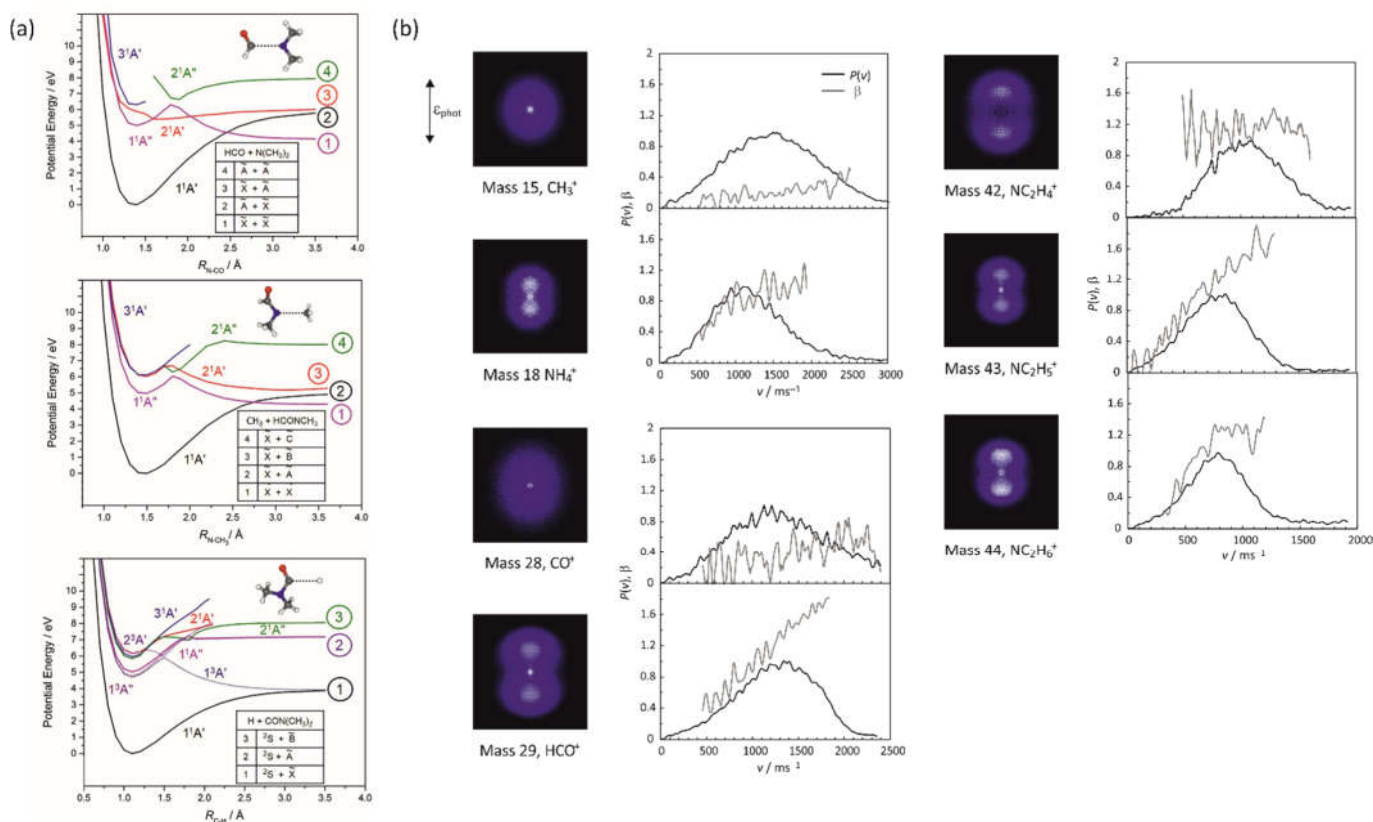


Figure 8: (a) Cuts through the first few adiabatic potential energy surfaces for for dissociation of N,N-DMF along the C-N, N-CH₃ and C-H bond coordinates (indicated by the dashed lines in the molecular structures); (b) velocity-map images and product speed and angular distributions for the observed fragmentation products. Reproduced with permission from reference 38.

NH_4^+ , and the least internally excited yield NC_2H_4^+ . The small effect of the dissociative ionisation step on the images for the detected fragments means that speed distributions extracted from the images for the $m/z = 16$, 42, and 43 fragments can be summed to obtain, at least to a very good approximation, the speed distribution that would have been obtained for the nascent $\text{N}(\text{CH}_3)_2$ fragment.

Following photofragment ionization at 118 nm, we do see the expected signal at $m/z = 29$, corresponding to the HCO product. However, we also see significant signal at $m/z = 28$, corresponding to CO. This is thought to be formed through predissociation of internally excited neutral HCO products, followed by 118 nm ionization of the resulting neutral CO fragments.

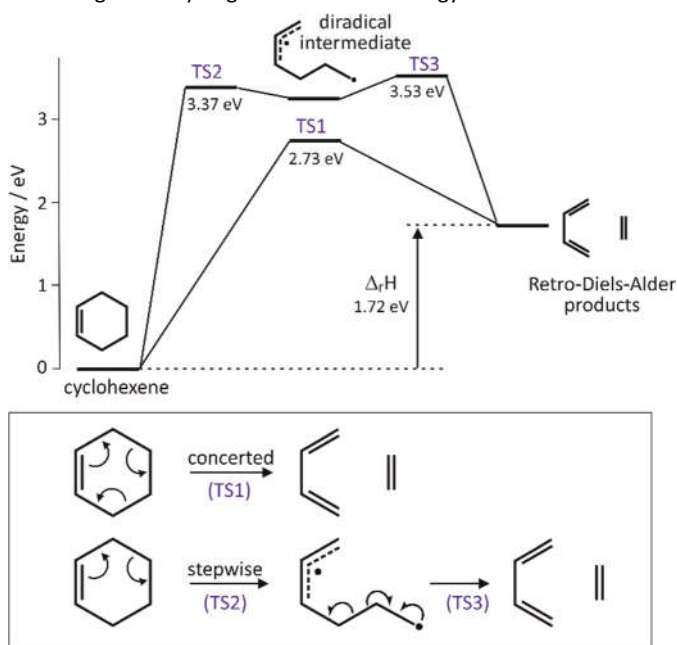
In addition to the signals above, arising from the 'peptide bond' dissociation channel, we also observe a strong signal at $m/z = 15$, corresponding to the CH_3 product of N- CH_3 bond cleavage. The partner fragment, $\text{N}(\text{CH}_3)\text{CHO}$, cannot be ionized at 118 nm, and is therefore not observed. We did not see evidence for direct H atom loss from electronically excited N,N-DMF, though we did see some evidence for H loss following internal conversion either of electronically excited parent molecules or of fragment molecules to highly vibrational excited levels of their respective ground states. We also observed H atoms thought to arise from secondary photolysis of some of the HCO fragments of N-C 'peptide' bond fission.

The observed products imply two main dissociation channels: cleavage of the N-C 'peptide' bond to form HCO and $\text{N}(\text{CH}_3)_2$ products; and cleavage of the N- CH_3 bond to form $\text{N}(\text{CH}_3)\text{HCO}$ and CH_3 products. Detailed analysis of the kinetic energy distributions extracted from the images, and in particular the energetic thresholds for formation of products in various electronic states, yields insight into the electronic states involved in these two dissociation pathways. Our data for the 'peptide' bond fission channel are consistent with initial population of the $3^1\text{A}'$ state of the parent, followed by internal conversion first to the $2^1\text{A}'$ state and then the $1^1\text{A}''$ state, which correlates with ground-state HCO and $\text{N}(\text{CH}_3)_2$ products. Two previous theoretical studies^{36,37} have also identified this as the dominant fragmentation pathway. In contrast with previous studies³⁵, we did not see any need to invoke additional minor pathways leading to formation of excited state products in order to explain our measured kinetic energy release distributions. The dissociation products arising from the peptide bond dissociation pathway are formed with significant internal excitation, implying rapid impulsive breaking of the bond.

The CH_3 loss channel is also thought to involve initial excitation to the $3^1\text{A}'$ state followed by radiationless population transfer to the $2^1\text{A}'$ state. From here, the molecule either dissociates on this surface, or undergoes a second radiationless transfer to the $1^1\text{A}''$ state. The two states correlate to ground-state CH_3 products partnered by $\text{N}(\text{CH}_3)\text{CHO}$ in its second excited (B) or ground (X) electronic state, respectively. The kinetic energy distribution for the products does not extend past the energetic limit for formation of B-state products, so is consistent with dissociation on the $2^1\text{A}'$ surface. However, the data would also be consistent with dissociation on the $1^1\text{A}''$ surface with formation of vibrationally and/or rotationally excited ground-state products.

3.3 Retro-Diels-Alder reaction.

The Diels-Alder reaction between a diene and a dienophile is a key reaction in the repertoire of a synthetic organic chemist, allowing formation of C-C bonds and creation of six-membered ring structures³⁹. The forward and reverse reactions also provide key examples of pericyclic reactions obeying the Woodward-Hoffman rules³⁹, which use frontier orbital symmetry to predict whether concerted pericyclic reactions are thermally or photochemically 'allowed' or 'forbidden', i.e. whether they have a low or a high activation barrier, respectively. For the Diels-Alder reaction, the Woodward-Hoffman rules predict that both the forward and reverse reactions are symmetry allowed on the ground-state potential energy surface, but symmetry forbidden on the first electronically excited state surface. In addition to the concerted mechanism, in which both C-C bonds break simultaneously, there is also the possibility of a stepwise mechanism leading to the same products. Both mechanisms are shown in Figure 9. The stepwise mechanism has a significantly higher activation energy than the concerted



mechanism.

Figure 9: Concerted and stepwise mechanisms for the retro-Diels-Alder reaction. TS1, TS2, and TS3 denote transition states. Adapted from reference 40.

We investigated the retro-Diels-Alder reactions of cyclohexene, 1-methylcyclohexene, and 4-methylcyclohexene following photoexcitation at 193 nm in a multimass VMI study⁴⁰. In all three cases, the products were found to be formed with isotropic angular distributions and with the majority of available energy released into internal degrees of freedom. As noted in Section 2.1.2, the lack of any anisotropy in the angular distribution is a hallmark of a relatively slow process occurring over a number of rotational periods. These observations are therefore consistent with a mechanism in which reaction occurs from high vibrational levels of the ground-state following internal conversion from the excited electronic state initially populated following absorption of a 193 nm photon. This

aligns with the predictions of frontier molecular orbital theory, and as noted by other authors^{41,42}, such a process most probably proceeds via a concerted rather than by a stepwise mechanism. The images recorded for the retro-Diels-Alder reaction products were very similar for all three molecules, indicating that methyl substitution at the 1 or 4 position of cyclohexene does not have any significant effect on the dynamics of the reaction.

One of the most important outcomes of this study is that it demonstrates the ability of VMI to provide insight into 'real' chemical reactions of interest to a wide audience of chemists. Multimass VMI has since been used to investigate ring-opening dynamics in bromocyclopropane⁴³ and 2-bromothiophene⁴⁴ and the UV photodissociation dynamics of dimethylsulphide⁴⁵, and will no doubt be used increasingly to perform detailed mechanistic studies on reactions of interest in synthetic organic photochemistry.

3.4. Ultra-fast pump-probe experiments

Femtosecond pump-probe experiments offer the exciting possibility of probing chemical processes directly on their natural timescale, and the growing field of femtochemistry has already provided unprecedented insight into many different areas of chemical dynamics⁴⁶.

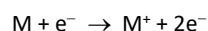
The readout system of the PlmMS camera was originally designed for multimass imaging experiments with nanosecond pulsed laser systems, which typically have repetition rates of 10 to 20 Hz. At present, the camera is not able to achieve the kHz readout rates that would make it optimally compatible with ultrafast laser experiments. However, though improving the readout speed of the PlmMS camera is still a work in progress, the multimass imaging capability is attractive enough that a number of different research groups around the world have already used the camera to perform ultrafast pump-probe VMI experiments. These include initial proof-of-concept experiments on C₂F₃I, carried out by Hockett and coworkers at the NRC in Ottawa⁴⁷, and a series of investigations into the photofragmentation and Coulomb explosion dynamics of various alkyl and aryl halides, performed by Rolles and coworkers at the FLASH free electron laser facility in Hamburg^{48,49,50,51}. While the experimental methodology still needs further development in order to exploit the approach to its full potential, these early studies have demonstrated that ultrafast time-resolved multimass VMI offers a powerful tool for investigating wavepacket dynamics on the femtosecond timescale, allowing the dynamics of multiple competing reaction channels to be resolved.

4. Electron-induced chemistry

Electron-molecule collisions can give rise to a variety of phenomena, depending on the collision energy. At low energy (<15 eV), collisions generally result in elastic and inelastic scattering, with dissociative or non-dissociative electron attachment also occurring at certain resonant energies. Above the ionization threshold for the molecule, ionization becomes important, with a variety of dissociative ionization pathways becoming accessible as the collision energy increases further. Our studies to date have focused on the latter regime, where electron ionization is the dominant process.

Electron ionization is one of the key ionization mechanisms within both naturally occurring and man-made plasmas, including industrial plasmas, gas discharges, fusion plasmas, planetary atmospheres, and interstellar gas clouds. It was the first ionization method employed in mass spectrometry, and is still in widespread use today in a variety of analytical instruments. Low energy secondary electrons generated through interactions of the primary radiation beam with tissue also play a key role in radiation damage to DNA and other biomolecules.

During the electron ionization process, the incoming electron, e⁻, 'knocks' an electron out of a molecule M, yielding a positive ion and two departing electrons:



A number of key parameters are required in order to understand the ionization process in detail. The first is the total ionization cross-section as a function of electron energy. This quantifies the probability of a collision leading to ionization, but does not provide any information on the fate of the newly-formed ion. This additional information is provided by partial ionization cross-sections, which quantify the probability of forming a particular fragment ion as a function of collision energy. Finally, the velocity distributions (i.e. scattering distributions) of the fragments provide information on partitioning of the available energy amongst the various available degrees of freedom of the fragment, as well as revealing any angular dependence of the dissociation process.

Two different types of measurements are required in order to measure the total and partial ionization cross-sections and the fragment scattering distributions. The total electron ionization cross-section⁵² is measured via a simple beam-gas experiment. An electron beam of tuneable energy is passed through a molecular gas of known pressure, generating positive ions via electron ionization. By recording the resulting positive ion current and the transmitted electron current as the electron energy is tuned over the desired range, together with the pressure and temperature of the gas, it is straightforward to determine the absolute electron ionization cross section over this energy range.

The partial ionization cross-sections and fragment scattering distributions are recorded using an electron-molecule crossed beam instrument with multi-mass velocity-map imaging detection. One important experimental modification that must be made in order to study interactions involving charged particles is that the interaction region must be free of electric or magnetic fields during the collisions. In a conventional VMI experiment for studying photoinitiated processes, the velocity-mapping field can be present continuously, as it does not affect the neutral photodissociation process under study, and the products only 'see' the electric field once they have been ionized, at which point they are rapidly extracted along the time-of-flight tube to the detector. In contrast, if the velocity-mapping field were to be present when a low-energy electron beam entered the interaction region, the beam would be steered straight into the repeller plate of the ion optics assembly rather than crossing the molecular beam to initiate the process of interest. The solution is to employ a pair of high-voltage switches, which allow the velocity-mapping lens elements to be held at ground potential while the electron beam traverses the interaction region,

before being rapidly switched to the required velocity-mapping voltages within a few nanoseconds of the electron beam clearing the lens assembly.

Relative partial ionization cross-sections are determined from a series of time-of-flight mass spectra recorded across a range of electron energies. Recall that the time of flight spectrum is obtained by integrating the multi-mass imaging data set recorded with a PImMS camera or similar over the spatial (x,y) coordinates. Combining these relative partial cross-sections with the absolute total cross-sections recorded using the beam-gas instrument, we are able to obtain absolute total and partial electron ionization cross-sections.

Having established the branching ratios into the various different fragmentation channels through the partial ionization measurements, the velocity-map images recorded for each fragment reveal details about the dynamics of the fragmentation process leading to each set of products. Interpreting the radial coordinate of the images is somewhat more difficult than for a photoinduced process. When a molecule absorbs a photon, the energy of the molecule is increased by a known amount, and it is usually straightforward to apply the principle of conservation of energy in order to investigate the energy balance within the products, and therefore to determine the total kinetic energy release for a given process if the kinetic energy of one fragment is known. In contrast, an electron-molecule collision can in principle transfer any energy up to the kinetic energy of the incident electron to the colliding molecule. For this reason, one can only reliably report kinetic energy distributions for individual products, and it is not generally possible to determine a total kinetic energy release for the process under study.

Despite these caveats, from the studies carried out so far, it is clear that even for molecules containing only a few atoms, collision with an electron leads to a wide variety of excitation and fragmentation dynamics occurring over a range of timescales. In the following, we consider two examples: SF_6 , and CF_3I .

4.1. Dissociative electron ionization of SF_6

SF_6 is used extensively as an etchant precursor in semiconductor manufacture^{53,54,55,56,57,58}, and quantitative information on fundamental ionization processes is useful in order to model and fine tune the etching process. Such information includes ion appearance thresholds, formation cross-sections, and kinetic energy distributions. All of these can be measured using the methods outlined above. In a recent publication⁵⁹, we reported the total ionization cross-section for SF_6 over the energy range from 0 to 300 eV, together with partial ionization cross-sections for formation of all observed ions. In order of decreasing abundance, the observed singly-charged ions were SF_5^+ , SF_3^+ , SF^+ , SF_2^+ , SF_4^+ , F^+ , and S^+ , implying a significant number of energetically accessible fragmentation channels at collision energies of a few tens of eV. A number of doubly charged ions - SF_4^{2+} , SF_2^{2+} , SF_3^{2+} , SF^{2+} , S^{2+} - were also observed at higher electron energies (above 50 eV), though these made up only a few percent of the total ion signal. Signal levels were sufficient to record velocity-map images for all ions apart from SF_2^{2+} and S^{2+} . These were recorded at 60 eV, 80 eV, and 100 eV for the singly charged ions, and 100 eV for the doubly charged ions. Example kinetic energy

distributions extracted from the images for the singly charged ions at a collision energy of 100 eV, together with a representative velocity-map image for the SF_5^+ fragment, are shown in Figure 10.

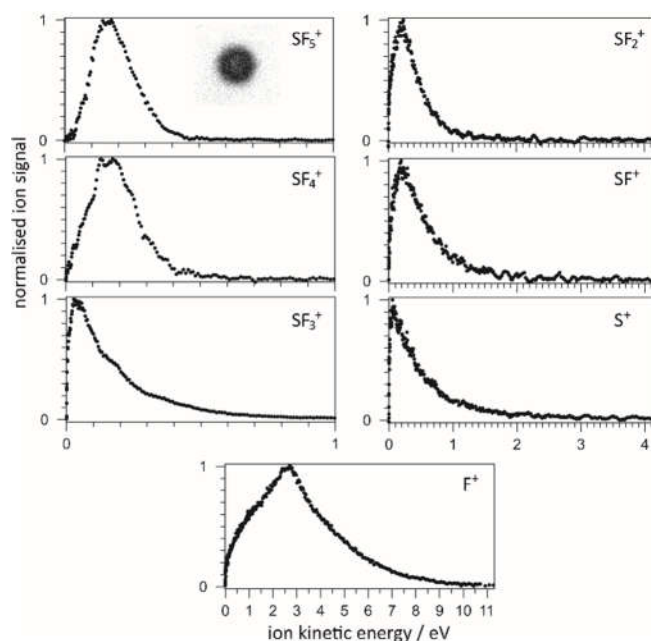


Figure 10: Kinetic energy distributions for the SF_5^+ , SF_4^+ , SF_3^+ , SF_2^+ , SF^+ , S^+ , and F^+ products of dissociative electron ionization of SF_6 . A representative velocity-map image for the SF_5^+ fragment is shown as an inset to the kinetic energy distributions. Adapted from reference 59.

Based on the molecules we have studied to date^{59,60,61}, a general feature of dissociative electron ionization appears to be that the kinetic energies of the fragments are very small relative to the incident electron energy. At most, a few percent of the incident electron energy appears as kinetic energy of the detected ionic fragment, implying that most of the energy transferred in the collision goes into overcoming the binding energy of the ionized electron and into kinetic energy of the two departing electrons, with only a very small amount of energy transferred into the rest of the molecular framework. The inefficient transfer of energy to the nuclear framework can be rationalised by considering the timescale over which the electron interacts with the molecule. The time taken for a 20 to 100 eV electron to traverse a molecular diameter is on the order of 10^{-17} to 10^{-16} s; this is well matched with the timescale of electronic motion, but several orders of magnitude faster than nuclear motion.

Detailed analysis of the images shown in Figure 10, aided by electronic structure calculations of the accessible electronic potential energy surfaces of the SF_6^+ cation, allows the dynamics of the various dissociation pathways to be unravelled. It is clear that multiple electronic states of SF_6 , SF_6^+ , and SF_6^{2+} play a role in the observed fragmentation dynamics. The measured kinetic energy distributions are consistent with rapid impulsive dissociation of the parent SF_6^+ ion to form SF_5^+ and SF_3^+ , the two most abundant ions.

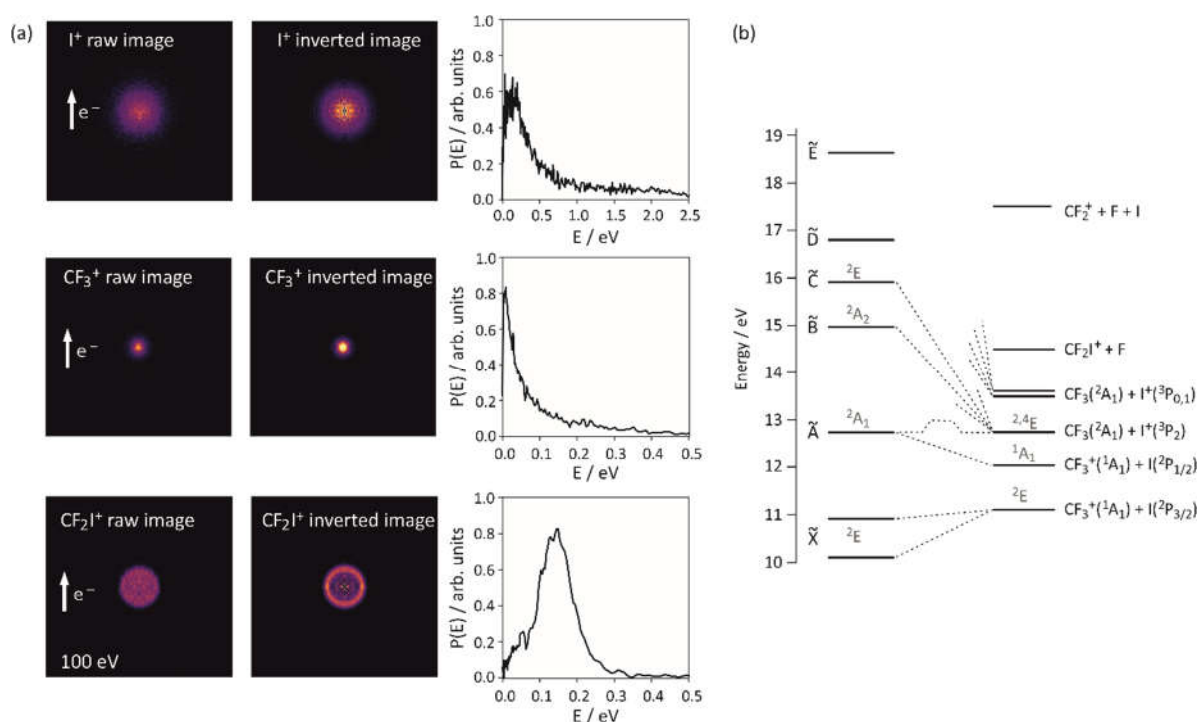


Figure 11: (a) Velocity-map images and kinetic energy distributions for the I^+ , CF_3^+ , and CF_2I^+ products of dissociative electron ionization of CF_3I at an electron energy of 100 eV; (b) partial correlation diagram for known electronic states of CF_3I^+ . For simplicity, the state symmetries are given in the C_{3v} point group only. Reference 56 also contains state symmetries in an extended point group representation. Adapted from reference 61.

The more highly internally excited of these ions then undergo much slower, 'statistical', loss of further fluorine atoms or F_2 , until internal energy in excess of the relevant SF_n^+ dissociation threshold has been liberated. In a similar way, the observed dications appear to result from initial formation of SF_n^{2+} followed by secondary dissociation over a longer timescale. Interestingly, there is very little dependence of the measured fragment ion kinetic energy distributions on the energy of the incident electron, implying that similar dissociative states are accessed across the entire 60 to 100 eV energy window studied.

The kinetic energy distributions for the observed singly-charged ions were also compared with the corresponding kinetic energy distributions arising from dissociative photoionization, measured in TPEPICO experiments (see reference 59 and references therein). There was found to be good agreement in all cases, implying either that both ionization methods populate similar excited states of the ion, or that the initially populated states undergo rapid internal conversion and/or intersystem crossing to a common set of dissociative states in both cases.

4.2. Dissociative electron ionization of CF_3I

Following on from the work on SF_6 , we have recently⁶¹ published a similar study on the dissociative electron ionization dynamics of CF_3I at energies ranging from 20 eV to 100 eV. In order of abundance based on the measured partial ionization cross-sections, the observed product ions are I^+ , CF_3I^+ , CF_3^+ , CF^+ , CF_2I^+ , CF_2^+ , C^+ , F^+ , and I_2^+ . This implies a number of energetically accessible fragmentation channels involving both C-F and C-I bond cleavage, in some cases

followed by further fragmentation of the resulting molecular ions. Velocity-map images were recorded for I^+ , CF_3^+ , and CF_2I^+ at electron energies of 40, 60, 80, and 100 eV. Representative images and kinetic energy distributions for these three ions at a collision energy of 100 eV are shown in Figure 11(a).

As seen for SF_6 , only a very small fraction, less than 1%, of the incident electron energy is released into kinetic energy of the fragments. The images also show little or no dependence on the electron energy. In common with SF_6 , this implies that the initially populated states of the CF_3I^+ ion rapidly relax to a common set of dissociative states. Additionally, it is observed that the images for products of C-F bond cleavage (CF_2I^+) have a markedly different appearance from those for the products of C-I bond cleavage (CF_3^+ and I^+).

Detailed analysis of the images, in the light of data from photoionization studies and known correlations between parent ion and fragment ion electronic states (see Figure 11(b)), provides further insight into the dissociation dynamics. The CF_3^+ images resulting from C-I bond cleavage imply a statistical dissociation mechanism occurring over relatively long timescales, while the significant kinetic energy release apparent in the images for the CF_2I^+ products of C-F cleavage suggests a much more direct dissociation involving one or more dissociative states of the parent ion, and occurring over much faster timescales. The I^+ ion shows behaviour intermediate between these two extremes. The CF_3^+ ion formed via dissociative electron ionization has a very similar kinetic energy distribution to CF_3^+ formed in dissociative photoionization^{55,57,58,62,63}, implying that it is most probably formed via statistical dissociation of CF_3I^+ in its electronic ground state. In contrast, the I^+ kinetic energy

distribution does not match well with those observed in photoionization studies. Most photoionization studies^{57,58,62,54,64} have assigned I^+ as being formed primarily via rapid impulsive dissociation from the \tilde{A} state of the CF_3I^+ ion. However, the low kinetic energy release observed for this ion in our work implies that it is formed via higher lying states, possibly the \tilde{D} and \tilde{E} states of CF_3I^+ , based on the correlation diagram in Figure 11(b). Finally, the CF_2I^+ ion is thought to form via C-F bond cleavage on the \tilde{B} , \tilde{C} , and \tilde{D} states of CF_3I^+ , yielding fragment kinetic energy distributions that are qualitatively similar to those observed in photodissociation studies^{54,57} on the CF_3I^+ cation via these states.

5. New tools for probing chemical dynamics: Coulomb-explosion and covariance-map imaging

In tandem with developments in multi-mass imaging, the past ten years or so has also seen rapid improvements in ultrafast laser technology, to the point where robust table-top femtosecond laser systems are now widely available and are used extensively in velocity-map imaging experiments. The past decade has also seen increasingly widespread access to beamtime at synchrotron light sources, free electron lasers, and other specialised facilities. These new technologies have led to a raft of new chemical dynamics experiments, many of which employ VMI detection. Perhaps one of the most exciting new techniques to spring from these opportunities is multi-mass Coulomb explosion imaging.

A Coulomb explosion occurs when a molecule rapidly loses a large number of valence electrons, essentially removing the chemical bonds between the atoms. The result is a set of positively charged atoms located at the same positions as in the original molecule. Extreme Coulomb repulsion between the atomic ions then rapidly leads to an 'explosion'. Coulomb explosions of small molecules have been studied for several decades⁶⁵. However, recent developments have made Coulomb explosion imaging a promising new method for gas-phase structure determination, with the potential to allow structural changes, and therefore chemical dynamics, to be followed in real time with femtosecond timing resolution. In principle, the technique offers a completely general probe step for dynamics experiments, with no intrinsic limitations to the type of molecule that can be studied.

During the Coulomb explosion, the initial positions of the atoms within the molecule are mapped onto the final velocities of the scattered ions. If the dynamics of the Coulomb explosion process are well understood, then measuring these velocities by VMI in principle allows one to work backwards to obtain the initial molecular structure. The electron-stripping step is usually achieved either through multiphoton/strong-field ionization with an intense (few mJ) femtosecond infra-red laser, or by X-ray ionization of a core electron followed by an Auger cascade. Both approaches have been used in multi-mass VMI investigations into Coulomb explosions^{48,49,50,67,69,70}, with a recent study⁴⁸ on difluoroiodobenzene showing that the two approaches lead to similar Coulomb explosion processes despite the very different initiation mechanisms.

The power of Coulomb explosion imaging is increased further using a data processing technique known as covariance mapping⁶⁶. As well as containing the velocity distribution of each detected fragment, a

multimass VMI data set also contains information about correlations between the velocity distributions of different fragments. Performing a statistical covariance analysis on the data allows these correlations to be revealed. Transforming the 'raw' velocity-map images into covariance images allows the velocity distribution of one product relative to one or more other fragments to be determined and visualised^{67,69,70}. This can reveal important details of both the structure of the molecule under study, and the dynamics of the Coulomb explosion process itself. Applications of covariance-map imaging are not restricted to Coulomb-explosion experiments: the approach will also prove extremely useful for untangling competing mechanisms in more conventional photodissociation studies by identifying covariances between species that are formed as product pairs. As a caveat, it is worth noting that covariance analysis will only be successful for experiments in which the ion detection efficiency is sufficiently high that there is a significant probability of detecting two (or more) products from a given chemical event. A considerable amount of experimental optimisation is often required in order to make sure that this is the case.

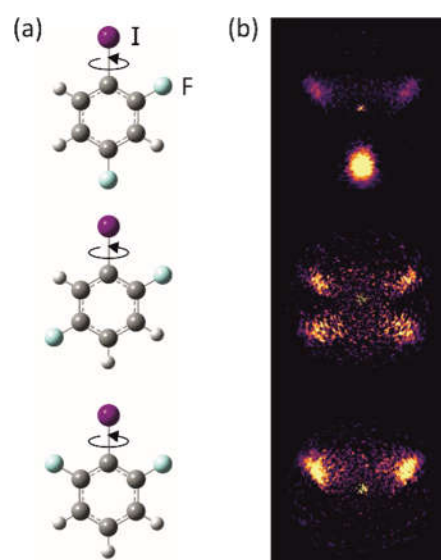


Figure 12: (a) Raw images for the Coulomb explosion products of 3,5-difluoroiodobenzene; (b) covariance-map images showing the F^+ fragment velocity distribution relative to I^+ . Note that the molecules are free to rotate about the C-I bond axis; hence the fluorine atom velocities appear to be mirrored about this axis. Adapted from reference 67.

As an example of Coulomb explosion and covariance-map imaging, we will briefly summarise a recent study in which the two techniques were used to distinguish between structural isomers of difluoroiodobenzene and dihydroxybromobenzene in the gas phase⁶⁷. Prior to Coulomb explosion, the electric field of an intense linearly-polarised nanosecond laser pulse was used to align the most polarisable molecular axis (containing the C-I bond) parallel to the plane of the image. Coulomb explosion was then initiated by a 30 fs pulse from a Ti:sapphire laser. Note that while the alignment laser fixes the molecular axis in space, the molecules are free to rotate about the alignment axis. The resulting covariance-map images for

the F^+ and I^+ products of the Coulomb explosion are shown in Figure 12(b) for 2,4-, 2,5-, and 2,6-difluoroiodobenzene. As noted above, during the Coulomb explosion, the initial atomic positions are mapped onto the final velocities of the atomic ions. I^+ has been chosen as the reference ion for the covariance analysis, and its velocity is fixed to point vertically upwards in the images. The covariance images show the velocity distributions for the F^+ fragments relative to the I^+ reference direction. The images for the three isomers are very different, and immediately allow the isomers to be distinguished from each other. When comparing the covariance images with the molecular structures, the observant reader will have noticed that the intensity distribution in the images appears to be a superposition of the intensity expected for the molecules as drawn, and for their mirror images. This apparent anomaly is easy to explain when we remember that the molecules are only aligned along one axis during the experiments, and are free to rotate about this axis. The images are therefore averaged over this rotational motion. In principle, this averaging could be removed by employing 2D, or even 3D, alignment of the parent molecules⁶⁸.

To date, covariance-map Coulomb explosion imaging has also been used to study the structure of a 1D-aligned substituted biphenyl molecule, and to image its vibrational motion in real time following infrared excitation^{69,70}. It has also been shown that three-fold covariance analysis can be used to establish the absolute configuration of a chiral molecule⁷¹.

6. Future work

Multi-mass VMI is still a very young technique, with much scope for further improvement and optimisation. From an experimental perspective, future developments in camera and ion detector technology will lead to improved ion detection sensitivity and time resolution, increasing the ability to resolve ions that are closely spaced in mass and to employ the covariance analysis methods described in Section 5. There is also considerable scope for developing new experimental techniques combining 3D slice imaging (see Section 2 and Figure 2) with covariance analysis in order to determine full correlated velocity distributions for reaction products in three dimensions. Such methods can be applied both to photodissociation experiments and to Coulomb explosions. We have very recently acquired the first proof-of-concept data for such an approach during a recent set of Coulomb explosion imaging experiments performed at the Artemis ultra-fast laser facility⁷². Figure 13 shows part of a preliminary 3D-sliced covariance-map imaging data set, in which the pairwise recoil of I^+ and CF_3^+ ions formed in the Coulomb explosion of CF_3I^{2+} is captured in three dimensions.

The use of Coulomb-explosion imaging as a method for following molecular structures is still in its infancy. At its present stage of development, the technique can provide useful structural details, particularly regarding bond angles, but is not yet able to deduce a detailed molecular structure from images of the Coulomb explosion products. In parallel with the experiments, we have been working hard over the past couple of years on developing forward-simulation codes that allow the Coulomb-explosion images to be predicted based on a trial molecular structure. The most recent versions of the

simulation software perform a complete *ab initio* calculation of the charge distribution within the molecule and the molecular forces at each step of a trajectory simulation. The trajectory simulation solves Newton's equations for the motion of the atoms subject to the molecular forces and the velocity-mapping field.

The simulations have already revealed some important insights into the use of Coulomb explosion imaging as a structural tool⁷³. These include indications relating to the relative usefulness of low and high charge states for structure determination, and the effect of vibrational and/or electronic excitation of the ion on the resulting Coulomb explosion. The eventual aim is to develop software that will allow users to provide an "initial guess" structure which can then be refined based on comparison with the experimental data to give a "best fit" structure.

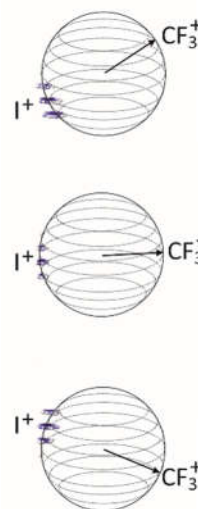


Figure 13: 3D-sliced covariance-map images of I^+ and CF_3^+ ions formed in the laser-induced Coulomb explosion of CF_3I^{2+} .

With some further development, Coulomb explosion imaging will offer a truly general probe step for chemical dynamics experiments, overcoming a number of limitations imposed by current techniques. As an example, isomerisation processes such as ring-opening or cis-trans isomerisation are very difficult to study via VMI, as they simply yield a rearranged version of the parent molecule, with no change in mass or velocity, rather than generating distinct photofragments whose velocity distribution is imprinted with the dynamics of the process under study. In contrast, Coulomb explosion imaging will allow the molecular structure to be imaged directly over the course of the isomerisation process.

6. Conclusions

Multi-mass velocity-map imaging is starting to become established as a promising method for probing the dynamics of a variety of gas-phase chemical processes. We have provided an overview of velocity-map imaging and multi-mass velocity-map imaging, and discussed a variety of examples in which these approaches have been used to study a range of photoinduced and electron-induced

chemical processes. Multi-mass VMI has also led to the development of two new tools for the chemical dynamics toolbox, in the form of Coulomb-explosion imaging and covariance-map imaging. Over the next few years, we believe that multi-mass VMI methods will become established as standard experimental techniques for use by the reaction dynamics community, allowing investigations into chemical processes relevant to disciplines ranging from atmospheric chemistry and astrochemistry through to synthetic organic photochemistry and biology.

Conflicts of interest

There are no conflicts to declare.

Acknowledgements

The author would like to thank the many colleagues who have shared the multimass imaging journey so far, in particular Mark Brouard and members of both of our research groups. Special thanks goes to Jason Lee and to our collaborators Renato Turchetta, Andrew Clarke, Andrei Nomerotski, Iain Sedgwick, James Bull, Henrik Stapelfeldt, Paul Hockett, Mike Ashfold, Andrew Orr-Ewing, Daniel Rolles, Rebecca Boll, and Melanie Schnell.

¹ See for example T. Okuyama and H. Maskill, *Organic Chemistry: a mechanistic approach* (Oxford University Press, Oxford, 2013, ISBN 978-0199693276); R. A. Y. Jones, *Physical and Mechanistic Organic Chemistry*, (Cambridge University Press, New York, 1980); B. K. Carpenter, *Determination of Organic Reaction Mechanisms* (Wiley Interscience, 1984, ISBN 978-0471893691); C. Vallance, *An Introduction to Chemical Kinetics* (Morgan and Claypool Publishers, 2017, ISBN 978-1-6817-4667-8).

² See for example P. L. Houston, *Chemical Kinetics and Reaction Dynamics* (Dover Publications Inc, 2006, ISBN 978-0486453347); R. D. Levine, *Molecular Reaction Dynamics* (Cambridge University Press, 2009, ISBN 978-0521140713); S. K. Upadhyay, *Chemical Kinetics and Reaction Dynamics* (Springer Netherlands, 2006, ISBN 978-1-4020-4546-2); M. Brouard and C. Vallance, *Tutorials in Molecular Reaction Dynamics* (RSC Publishing, Cambridge, 2011, ISBN 978-1-84973-530-8); M. Brouard, *Reaction Dynamics* (Oxford Chemistry Primers, Oxford University Press, USA, 1998, ISBN 978-0198559078).

³ R. G. J. Fraser and L. F. Broadway, *Proc. Royal Soc. A*, 1933, **141**, <http://doi.org/10.1098/rspa.1933.0143>; E. H. Taylor and S. Datz, *J. Chem. Phys.*, 1955, **23**(9), 1711; W. B. Miller, S. A. Safron, D. R. Herschbach, *Discuss. Faraday Soc.*, 1967, **44**, 108; Y. T. Lee, *Science*, 1987, **236**, 4803; D. Herschbach, *Annu. Rev. Phys. Chem.*, 2000, **51**, 1.

⁴ M. Brouard, P. O'Keeffe, and C. Vallance, *J. Phys. Chem. A*, 2002, **106**(15), 3629, and references therein;

⁵ W. R. Simpson, A. J. Orr-Ewing, T. P. Rakitzis, S. A. Kandel, and R. N. Zare, *J. Chem. Phys.*, 1995, **103**(17), 7299; L. Schnieder, K. Seekamp, J. Borkowski, E. Wrede, K. H. Welge, F. J. Aoiz, L. Banares, M. J. Dmello, V. S. Rabanos, and R. E. Wyatt, *Science*, 1995, **269**, 207; T. P. Softley, *Int. Rev. Phys. Chem.*, 2004, **23**(1), 1.

⁶ A. T. J. B. Eppink and D. H. Parker, *Rev. Sci. Instrum.*, 1997, **68**, 3477.

⁷ D. W. Chandler and P. L. Houston, *J. Chem. Phys.*, 1987, **87**, 1445.

⁸ F. J. Aoiz, M. Brouard, S. D. S. Gordon, B. Nichols, S. Stolte, and V. Walpole, *Phys. Chem. Chem. Phys.*, 2015, **17**, 30210, and references therein;

⁹ H. Pan, K. Liu, A. Caracciolo, and P. Casavecchia, *Chem. Soc. Rev.*, 2017, **46**, 7517, and references therein.

¹⁰ J. Mikosch, U. Fruhling, S. Trippel, D. Schwalm, M. Weidemuller, and R. Wester, *Phys. Chem. Chem. Phys.*, 2006, **8**, 2990; J. Mikosch, S. Trippel, C. Eichhorn, R. Otto, U. Lourderaj, J. X. Zhang, W. L. Hase, M. Weidemuller, and R. Wester, *Science*, 2008, **319**, 183; J. Zhang, J. Mikosch, S. Trippel, R. Otto, M. Weidemuller, R. Wester, and W. L. Hase, *J. Phys. Chem. Lett.*, 2010, **1**, 2747; J. Mikosch, M. Weidemuller, and R. Wester, *Int. Rev. Phys. Chem.*, 2010, **29**, 589; R. Otto, J. Brox, S. Trippel, M. Stei, T. Best, and R. Wester, *Nature Chemistry*, 2012, **4**, 534; R. Wester, *Phys. Chem. Chem. Phys.*, 2014, **16**, 396; L. Pei, E. Carrascosa, N. Yang, S. Fancinelli, and J. M. Farrar, *J. Phys. Chem. Lett.*, 2015, **6**, 1684; M. Stei, E. Carrascosa, M. A. Kainz, A. K. Kelkar, J. Meyer, I. Szabo, G. Czako, and R. Wester, *Nature Chemistry*, 2016, **8**, 151; J. Meyer and R. Wester, *Annu. Rev. Phys. Chem.*, 2017, **68**, 333; E. Carrascosa, J. Meyer, J. Zhang, M. Stei, T. Michaelson, W. L. Hase, L. Yang, and R. Wester, *Nature Commun.*, 2017, **8**, 25; E. Carrascosa, J. Meyer, and R. Wester, *Chem. Soc. Rev.*, 2017, **46**, 7498.

¹¹ E. W. Hansen and P.-L. Law, *J. Opt. Soc. Am. A*, 1985, **2**(4), 510; E. W. Hansen, *IEEE Trans. Acoust. Speech Signal Proc.*, 1985, **33**, 666; C. J. Dasch, *Applied Optics*, 1992, **31**(8), 1146; C. Bordas and F. Paulig, *Rev. Sci. Instrum.*, 1996, **67**, 2257; V. Dribinski, A. Ossadtchi, V. A. Mandelshtam, and H. Reisler, *Rev. Sci. Instrum.*, 2002, **73**(7), 2634; G. M. Roberts, J. L. Nixon, J. Lecointre, E. Wrede, and J. R. Verlet, *Rev. Sci. Instrum.*, 2009, **80**, 053104; T. Gerber, Y. Liu, G. Knopp, P. Hemberger, A. Bodi, P. Radi, and Y. Sych, *Rev. Sci. Instrum.*, 2013, **84**(3), 033101; C. E. Rallis, T. G. Burwitz, P. R. Andrews, M. Zohrabi, R. Averin, S. De, A. Bergues, B. Jochim, A. V. Voznyuk, N. Gregerson, B. Gaire, I. Znakovskaya, J. McKenna, K. D. Carnes, M. F. Kling, I. Ben-Itzhak, and E. Wells, *Rev. Sci. Instrum.*, 2014, **85**, 113105.

¹² C. R. Gebhardt, T. P. Rakitzis, P. C. Samartzis, V. Ladopoulos, and T. N. Kitsopoulos, *Rev. Sci. Instrum.*, 2001, **72**(10), 3848; L. Dinu, A. T. J. B. Eppink, F. Rosca-Pruna, H. L. Offerhaus, W. J. van der Zande, and M. J. J. Vrakking, *Rev. Sci. Instrum.*, 2002, **73**(12), 4206; D. Townsend, M. P. Minitti, and A. G. Suits, *Rev. Sci. Instrum.*, 2003, **74**(4), 2350; J. J. Lin, J.

- Zhou, W. Shiu, and K. Liu, *Rev. Sci. Instrum.*, 2003, **74**(4), 2495.
- ¹³ B.-Y. Chang, R. C. Hoetzlein, J. A. Mueller, J. D. Geiser, and P. L. Houston, *Rev. Sci. Instrum.*, 1998, **69**, 1665; W. Li, S. D. Chambreau, S. A. Lahankar, and A. Suits, *Rev. Sci. Instrum.*, 2005, **76**, 063106.
- ¹⁴ M. Ashfold, D. Chestakov, I. Garcia, T. Kitsopoulos, N. Nahler, A. Orr-Ewing, D. Parker, R. Toomes, O. Vieuxmaire, and S.-M. Wu, *Phys. Chem. Chem. Phys.*, 2006, **8**, 26; D. Chandler and A. Heck, *Ann. Rev. Phys. Chem.*, 1995, **46**, 335; P. Houston, *Acc. Chem. Res.*, 1995, **28**, 453; A. G. Suits and R. E. Continetti, *Imaging in Chemical Dynamics* (ACS Symposium Series, Vol. 770, American Chemical Society, Washington D. C., 2001); B. J. Whitaker, *Imaging in Molecular Dynamics: Technology and Applications* (Cambridge University Press, Cambridge, 2003).
- ¹⁵ M. J. Bass, M. Brouard, A. P. Clark, B. Martinez-Haya, and C. Vallance, *Phys. Chem. Chem. Phys.*, 2003, **5**, 856.
- ¹⁶ T. P. Rakitzis and T. N. Kitsopoulos, *J. Chem. Phys.*, 2002, **116**, 9228.
- ¹⁷ A. S. Bracker, E. R. Wouters, A. G. Suits, and O. S. Vasyutinski, *J. Chem. Phys.*, 1999, **110**, 6749.
- ¹⁸ Y. Matsumi, K. Tonokura, and M. Kawasaki, *J. Chem. Phys.*, 1992, **97**, 1065.
- ¹⁹ P. C. Samartzis, T. Gougousi, and T. N. Kitsopoulos, *Laser Chemistry*, 1997, **17**, 185.
- ²⁰ P. C. Samartzis, B. L. G. Bakker, T. P. Rakitzis, D. H. Parker, and T. N. Kitsopoulos, *J. Chem. Phys.*, 1999, **110**, 5201.
- ²¹ R. N. Zare, *Angular Momentum: Understanding Spatial Aspects in Chemistry and Physics* (ISBN-13 978-0471858928, John Wiley and Sons, 1988)
- ²² See for example A. J. Orr-Ewing, *J. Chem. Soc. Faraday Trans.*, 1996, **92**, 881; A. P. Clark, M. Brouard, F. Quadrini, and C. Vallance, *Phys. Chem. Chem. Phys.*, 2006, **8**, 5591; C. Vallance, *Phys. Chem. Chem. Phys.*, 2011, **13**, 14427.
- ²³ S.-M. Wu, D. Chestakov, G. Wu, X. Yang, C. Vallance, G. C. Groenenboom, W. J. van der Zande, and D. H. Parker, *Molecular Physics*, 2010, **108**(7), 1145.
- ²⁴ S.-M. Wu, D. C. Radenovic, W. J. van der Zande, G. C. Groenenboom, D. H. Parker, C. Vallance, and R. N. Zare, *Nature Chemistry*, 2011, **3**, 28.
- ²⁵ H. Kung, J. F. Young, and S. E. Harris, *Appl. Phys. Lett.*, 1973, **22**, 301; H. Kung, J. F. Young, and S. E. Harris, *Appl. Phys. Lett.*, 1976, **28**, 294; P. Lockyer and J. C. Vickerman, *Laser Chem.*, 1997, **17**, 139.
- ²⁶ M. Brouard, E. K. Campbell, A. J. Johnsen, C. Vallance, W. H. Yuen, and A. Nomerotski, *Rev. Sci. Instrum.*, 2008, **79**, 123115.
- ²⁷ A. Nomerotski, M. Brouard, E. Campbell, A. Clark, J. Crooks, J. Fopma, J. J. John, A. J. Johnsen, C. Slater, R. Turchetta, C. Vallance, E. Wilman, and W. H. Yuen, *J. Inst.*, 2010, **5**, C07007/0-6.
- ²⁸ C. Vallance, M. Brouard, A. Lauer, C. Slater, E. Halford, B. Winter, S. J. King, J. W. L. Lee, D. Pooley, I. Sedgwick, R. Turchetta, A. Nomerotski, J. J. John, and L. Hill, *Phys. Chem. Chem. Phys.*, 2013, **16**, 383.
- ²⁹ X. Llopart, R. Ballabriga, M. Campbell, L. Tlustos, and W. Wong, *Nucl. Instrum. Meth. A*, 2007, **581**(1-2), 485.
- ³⁰ See for example J. H. Jungmann, A. Gijbertsen, J. Visser, J. Visschers, R. M. A. Heeren, and M. J. J. Vrakking, *Rev. Sci. Instrum.*, 2010, **81**, 103112; G. Gademann, Y. Huisman, A. Gijbertsen, J. Jungmann, J. Visschers, and M. J. Vrakking, *Rev. Sci. Instrum.*, 2009, **80**, 103105.
- ³¹ C. A. Taatjes, D. L. Osborn, T. M. Selby, G. Meloni, H. Fan, and S. T. Pratt, *J. Phys. Chem. A*, 2008, **112**, 9336; A. T. J. B. Eppink and D. H. Parker, *J. Chem. Phys.*, 1998, **109**(12), 4758; T. F. Hunter and K. S. Kristjansson, *Chem. Phys. Lett.*, 1978, **58**(2), 291; R. K. Sparks, K. Shobatake, L. R. Carlson, and Y. T. Lee, *J. Chem. Phys.*, 1981, **75**(8), 3838; M. D. Barry and P. A. Gorry, *Molecular Physics*, 1984, **52**(2), 461; A. T. J. B. Eppink and D. H. and Parker, *Rev. Sci. Instrum.*, 1997, **68**(9), 3477; A. T. J. B. Eppink and D. H. Parker, *J. Chem. Phys.*, 1999, **110**(2), 832; M. G. González, J. D. Rodríguez, L. Rubio-Lago, G. A. García, and L. Bañares, *Phys. Chem. Chem. Phys.*, 2011, **13**(36), 16404; R. de Nalda, J. G. Izquierdo, J. Durá, and L. Bañares, *J. Chem. Phys.*, 2007, **126**(2), 021101; R. De Nalda, J. Durá, G. A. García, J. G. Izquierdo, J. González-Vázquez, and L. Bañares, *J. Chem. Phys.*, 2008, **128**(24), 244309.
- ³² S. H. Gardiner, M. L. Lipciuc, T. N. Karsili, M. N. R. Ashfold, and C. Vallance, *Phys. Chem. Chem. Phys.*, 2015, **17**, 4096.
- ³³ R. S. Mulliken, *Phys. Rev.*, 1936, **50**, 1017; R. S. Mulliken, *J. Chem. Phys.*, 1940, **8**, 382.
- ³⁴ N. R. Forde, T. L. Myers, and L. J. Butler, *Faraday Discuss.*, 1997, **108**, 221.
- ³⁵ N. R. Forde, L. J. Butler, and S. A. Abrash, *J. Chem. Phys.*, 1999, **110**, 8954.
- ³⁶ D. Liu, W. Fang, Z. Lin, and X. Fu, *J. Chem. Phys.*, 2002, **117**, 9241.
- ³⁷ M. Eckert-Maksic and I. Antol, *J. Phys. Chem. A*, 2009, **113**, 12582.
- ³⁸ M. L. Lipciuc, S. H. Gardiner, J. W. L. Lee, T. N. V. Karsili, M. N. R. Ashfold, and C. Vallance, *J. Chem. Phys.*, 2017, **147**, 013941.
- ³⁹ G. Clayden, S. Warren, N. Greeves, and P. Wothers, *Organic Chemistry* (Oxford University Press, Oxford, UK, 2000).
- ⁴⁰ S. H. Gardiner, M. L. Lipciuc, and C. Vallance, *J. Phys. Chem. A*, 2015, **119**, 12218.
- ⁴¹ W. Fuss, W. E. Schmid, and S. A. Trushin, *J. Am. Chem. Soc.*, 2001, **123**, 7101.
- ⁴² X. Zhao, R. E. Continetti, A. Yokoyama, E. J. Hinsta, and Y. T. Lee, *J. Chem. Phys.*, 1989, **91**, 4118.
- ⁴³ S. Pandit, T. J. Preston, S. J. King, C. Vallance, and A. J. Orr-Ewing, *J. Chem. Phys.*, 2016, **144**, 244312.
- ⁴⁴ R. A. Ingle, C. S. Hansen, E. C. Elsdon, M. Bain, S. J. King, J. W. L. Lee, M. Brouard, C. Vallance, R. Turchetta, and M. N. R. Ashfold, *J. Chem. Phys.*, 2017, **147**, 013914.
- ⁴⁵ M. Bain, C. S. Hansen, and M. N. Ashfold, *J. Chem. Phys.*, 2018, **149**, 081103.
- ⁴⁶ A. H. Zewail, *Femtochemistry: Ultrafast Dynamics of the Chemical Bond, Volumes I and II* (World Scientific Series in 20th Century Chemistry, Volume 3, World Scientific

Publishing Company, 1994); *Ultrafast Phenomena in Molecular Sciences: Femtosecond Physics and Chemistry*, Edited by Rebeca de Nalda and Luis Bañares (Springer Series in Chemical Physics, Springer International Publishing, Switzerland, 2014).

⁴⁷ R. Forbes, V. Makhija, K. Veyrinas, A. Stollow, J. W. L. Lee, M. Burt, M. Brouard, C. Vallance, I. Wilkinson, R. Lausten, and P. Hockett, *J. Chem. Phys.*, 2017, **147**, 013911.

⁴⁸ K. Amini, R. Boll, A. Lauer, M. Burt, J. W. L. Lee, L. Christensen, F. Brausse, T. Mullins, E. Savelyev, U. Ablikim, N. Berrah, C. Bomme, S. Düsterer, B. Erk, H. Höppner, P. Johnsson, T. Kierspel, F. Krecinic, J. Küpper, M. Müller, E. Müller, H. Redlin, A. Rouzée, N. Schirmel, J. Thøgersen, S. Techert, S. Toleikis, R. Tresch, S. Trippel, A. Ulmer, J. Wiese, C. Vallance, A. Rudenko, H. Stapelfeldt, M. Brouard, and D. Rolles, *J. Chem. Phys.*, 2017, **147**, 7.

⁴⁹ M. Burt, R. Boll, J. W. L. Lee, K. Amini, H. Köckert, C. Vallance, A. Gentleman, S. Mackenzie, S. Bari, C. Bomme, S. Düsterer, B. Erk, B. Manschwetus, E. Müller, D. Rompotis, E. Savelyev, N. Schirmel, S. Techert, R. Treusch, and D. Rolles, *Phys. Rev. A*, 2017, **96**, 043415.

⁵⁰ E. Savelyev, K. Amini, F. Brausse, N. Berrah, C. Bomme, M. Brouard, M. Burt, L. Christensen, S. Düsterer, B. Erk, H. Höppner, T. Kierspel, F. Krecinic, A. Lauer, J. W. L. Lee, M. Müller, E. Müller, T. Mullins, H. Redlin, N. Schirmel, J. Thøgersen, S. Techert, S. Toleikis, R. Treusch, S. Trippel, A. Ulmer, C. Vallance, J. Wiese, P. Johnsson, J. Küpper, A. Rudenko, A. Rouzée, H. Stapelfeldt, D. Rolles, and Rebecca Boll, *Structural Dynamics*, 2018, **5**, 014301.

⁵¹ F. Allum, M. Burt, K. Amini, R. Boll, H. Köckert, P. K. Olshin, S. Bari, C. Bomme, F. Brausse, B. Cunha de Miranda, S. Düsterer, B. Erk, M. Geleoc, R. Geneaux, A. S. Gentleman, G. Goldsztejn, R. Guillemin, D. M. P. Holland, I. Ismail, P. Johnsson, L. Journal, J. Kupper, J. Lahl, J. W. L. Lee, S. Maclot, S. R. Mackenzie, B. Manschwetus, A. S. Mereshchenko, R. Mason, J. Palaudoux, M. N. Piancastelli, F. Penent, D. Rompotis, A. Rouzee, T. Ruchon, A. Rudenko, E. Savelyev, M. Simon, N. Schirmel, H. Stapelfeldt, S. Techert, O. Travnikova, S. Trippel, J. G. Underwood, C. Vallance, J. Wiese, F. Ziaee, M. Brouard, T. Marchenko, and D. Rolles, *J. Chem. Phys.*, 2018, **149**, 204313.

⁵² P. W. Harland and C. Vallance, *Positive ion - electron impact ionization cross sections: theory and experiment*, [319-358 in *Advances in Gas Phase Ion Chemistry Volume 3*, Edited by N. G. Adams and L. M. Babcock (J. A. I. Press Inc. 1998).

⁵³ L. G. Christophorou and J. K. Olthoff, *Fundamental Electron Interactions with Plasma Processing Gases*, (Kluwer Academic/Plenum Publishers, New York, 2004).

⁵⁴ L. G. Christophorou and J. K. Olthoff, *J. Phys. Chem. Ref. Data*, 2000, **29**, 267.

⁵⁵ V. M. Donnelly and A. Kornblit, *J. Vac. Sci. Tech. A*, 2013, **31**, 050825.

⁵⁶ G. S. Oehrlein and J. F. Rembetski, *IBM J. Res. Develop*, 1992, **39**, 140.

⁵⁷ B. Wu, A. Kumar and S. Pamarthy, *J. Appl. Phys.*, 2010, **108**, 051101.

⁵⁸ S. Banna, A. Agarwal, G. Cunge, M. Darnon, E. Pargon and O. Joubert, *J. Vac. Sci. Technol. A*, 2012, **30**, 040801.

⁵⁹ J. N. Bull, J. W. L. Lee, and C. Vallance, *Phys. Rev. A*, 2017, **96**, 042704.

⁶⁰ J. N. Bull, J. W. L. Lee, and C. Vallance, *Phys. Rev. A*, 2015, **91**, 022704.

⁶¹ H. Koeckert, D. Heathcote, J. W. L. Lee, W. Zhou, V. Richardson, and C. Vallance, *Phys. Chem. Chem. Phys.*, published online January 2019, DOI: 10.1039/C8CP06682E.

⁶² G. G. Raju, *Gaseous electronics: tables, atoms, and molecules* (CRC Press, 2012).

⁶³ B. G. Lindsay and M. A. Mangan, *Photon- and Electron-Interactions with Molecules: Ionization and Dissociation (Chapter 5: Ionization)*, Y. Itikawa, Ed., (Springer, New York, 2003).

⁶⁴ T. D. Märk, *Contrib. Plasma Phys.*, 1982, **22**, 257.

⁶⁵ T. Yatsushashi and N. Nakashima, *J. Photochem. Photobiol. C: Photochemistry Reviews*, 2018, **34**, 52, and references therein.

⁶⁶ L. J. Frasinski, *J. Phys. B.*, 2016, **49**, 152004.

⁶⁷ M. Burt, K. Amini, J. W. L. Lee, L. Christiansen, R. R. Johansen, Y. Kobayashi, J. D. Pickering, C. Vallance, M. Brouard, and H. Stapelfeldt, *J. Chem. Phys.*, 2018, **148**, 091102.

⁶⁸ H. Stapelfeldt and T. Seideman, *Rev. Mod. Phys.*, 2003, **75**, 543.

⁶⁹ C. S. Slater, S. Blake, M. Brouard, A. Lauer, C. Vallance, J. J. John, R. Turchetta, A. Nomerotski, L. Christensen, J. H. Nielsen, M. P. Johansson, and H. Stapelfeldt, *Phys. Rev. A*, (2014), **89**, 011401(R).

⁷⁰ C. S. Slater, S. Blake, M. Brouard, A. Lauer, C. Vallance, C. S. Bohun, L. Christensen, J. H. Nielsen, M. P. Johansson, and H. Stapelfeldt, *Phys. Rev. A*, 2015, **91**, 053424.

⁷¹ L. Christensen, J. H. Nielsen, C. S. Slater, A. Lauer, M. Brouard, and H. Stapelfeldt, *Phys. Rev. A*, 2015, **92**, 033411.

⁷² J. W. L. Lee, J. Köckert, D. Heathcote, D. Popat, R. Chapman, P. Majchrzak, E. Springate, and C. Vallance, in preparation 2019.

⁷³ W. Zhou, L. Ge, G. Cooper, M. Evans, M. N. R. Ashfold, and C. Vallance, in preparation 2019.